Analyst

Fast quantification of nanorod geometry by DMA-spICP-MS

Journal:	*Analyst*
Manuscript ID	AN-ART-11-2018-002250.R1
Article Type:	Paper
Date Submitted by the Author:	15-Feb-2019
Complete List of Authors:	Tan, Jiaojie; National Institute of Standards and Technology, Materials Measurement Science Division; University of Maryland Yang, Yong; University of Maryland El Hadri, Hind; National Institute of Standards and Technology, Materials Measurement Science Division Li, Mingdong; University of Maryland Hackley, Vincent; NIST, Materials Measurement Science Division Zachariah, Michael; University of Maryland at College Park,

Fast quantification of nanorod geometry by DMA-spICP-MS

Jiaojie Tan [1,2], Yong Yang[2], Hind El Hadri[1], Mingdong Li[3], Vincent A. Hackley*[1], and Michael R. Zachariah*[2,3]

1. Materials Measurement Science Division, National Institute of Standards and Technology, Gaithersburg, Maryland 20899, United States
2. University of Maryland, College Park, Maryland 20742, United States.
3. Chemical Sciences Division, National Institute of Standards and Technology, Gaithersburg, Maryland 20899, United States

Abstract

A fast, quantitative method for determining the dimensions of nanorods (i.e., length and diameter) is described, based on hyphenation of differential mobility analysis (DMA) with single particle inductively coupled plasma mass spectrometry (spICP-MS). Seven gold nanorod samples with different dimensions (diameters 11.8 nm to 38.2 nm, aspect ratios 1.8 to 6.9) were used to validate the method. We demonstrate that DMA-spICP-MS can (1) achieve quantification of both length and diameter comparable with TEM analysis, (2) make statistically meaningful measurements in minutes at low concentrations (< 10^8/mL) and (3) separate nanorods from spheres and quantify the geometry of each population. A robustness analysis of this method was performed to evaluate potential biases in this approach.

Introduction

Rod-shaped metallic nanoparticles (nanorods) are increasingly applied in across a range of fields including biomedicine, catalysis and electronics [1-5]. In particular, gold nanorods (GNRs) have been used in diagnostics,[6] biosensors,[7] and hyperthermal therapy[8], due to their size-dependent localized surface plasmon resonance (SPR). Rod-shaped metal oxides, such as Fe_3O_4, CeO_2, TiO_2 and others have been employed as catalysts or essential components for heterogeneous catalysis applications.[1] The critical dimensions (i.e., length and diameter) of the rod are crucial in determining the properties of interest, and can influence final utilization. Therefore, the control of dimensions during synthesis and post-synthesis requires rapid and reliable analytical tools, which are currently scarce beyond imaging approaches.

Transmission electron microscopy (TEM) is the most frequently used method to obtain dimensions of nanorods; however, a sufficiently large number of particles, N, must be counted to obtain statistically reliable results (i.e., measurement precision increases in proportion to $\sqrt{N}$), which can be costly and laborious. Furthermore, artifacts such as aggregation can be produced during sample preparation and can complicate image analysis.

Efforts have also been made to relate GNR dimensions to unique spectral features. [9-13]. For instance, Link et al. [9] modeled the optical absorption spectra of GNRs and derived a simple relationship between the longitudinal SPR (LSPR) absorption maximum and the aspect ratio (AR). The extraction of geometric parameters is primarily based on electromagnetic modeling and with

the assistance of *a priori* knowledge of mean diameter and end shape. [14-16] Hu et al. [17] developed a more convenient method from spectral fitting by establishing LSPR relations for GNRs, and achieved reliable results. However, such simulations require significant expertise in the fundamental theories and therefore are not widely available to non-experts. Applications are limited to well-defined GNRs, and are not readily extendable to non-SPR associated nanorods, such as hybrid metal rods or metal oxides. This approach becomes considerably more complex and less accurate when dealing with a mixture of geometries or length/diameter distributions.

In prior work [18, 19] we have employed ion-mobility methods coupled to inductively coupled plasma mass spectrometry (ICP-MS). The differential mobility analyzer (DMA) is a type of ion-mobility spectrometer that classifies particles based on mobility size in the range from 2 nm to hundreds of nm. Depending on the operational conditions, a DMA can achieve a resolution up to 100:1 (capable of differentiating a 1 % difference in mobility). [20] The DMA can also be used as a band pass filter to select one specific mobility size, which can be passed to another instrument or detector. Theories investigating ion mobility of non-spherical nanoparticles have been extensively studied. [21] For cylindrical shaped particles in particular, the exact analytical expression of mobility depends on two geometric parameters, diameter and length (d_r and L_r). Zachariah and coworkers [22, 23], for example, developed a pulsed DMA to obtain geometry information by systematically changing the alignment of nanorods using a varying electric field to vary mobility. This method, however, requires the nanorods to be conductive in order to align in the applied field.

Single particle ICP-MS (spICP-MS) is an emerging technique with the capability of simultaneously determining both the concentration and mass of metal nanoparticles. In comparison to traditional ICP-MS, spICP-MS utilizes very fast acquisition times (μs) to capture single particle events, and therefore is capable of characterization on a "particle by particle" basis. Each particle is presented as an ion-mass resolved intensity directly proportional to the mass of the particle ionized in the plasma. For a cylindrical shaped particle, mass is a function of d_r and L_r, so combining the independent information from mobility (i.e., derived from DMA measurement) with mass (i.e., derived from spICP-MS), d_r and L_r are theoretically calculable and can be performed in a single hyphenated measurement. An analogous, though off-line approach, was explored by Nguyen et al., [24] where fractions from a polydisperse commercial GNR sample were collected following separation by asymmetric flow field-flow fractionation. Off-line analysis of fractions was performed using spICP-MS to extract length; the diameter was obtained from independent TEM imaging and assumed constant in this study (GNRs were grown from the same seed size).

We have previously explored tandem analysis with DMA and spICP-MS for simultaneous and accurate measurement of size, mass and concentration, and validation using NIST Au nanoparticle reference materials.[19, 25] In this proof-of-principle study, we extend our previous work to non-spherical particles and the simultaneous characterization of GNR diameter and length, while demonstrating the capacity to obtain statistically meaningful measurements in minutes at very low particle concentrations (10^5 to 10^8)/mL. Finally, we use this hyphenated approach to distinguish nanorod populations from spherical/non-nanorod impurities in a mixture, a measurement critical for manufacturing quality control.

Experimental

Materials

Cetyltrimethylammonium bromide (CTAB) stabilized GNRs in aqueous suspension were obtained from Nanopartz (Loveland, CO, USA)† and citrate stabilized GNRs were obtained from NanoComposix (San Diego, CA, USA). LSPR bands for the GNRs range from 600 nm to 1400 nm. The naming scheme presented in Table 1 indicates the surface coating and the LSPR. For example, CIT-660 refers to citrate capped GNRs with LSPR at 660 nm. There are two GNR samples with LSPR at 850 nm, but they differ in diameter (20 nm and 40 nm). To distinguish between these two, we included their diameters in the sample name: *viz.* CTAB-20-850 and CTAB-40-850.

NIST Reference Material 8013 (RM8013, Gold Nanoparticles, Nominal 60 nm Diameter) was used as a calibration standard for spICP-MS. NIST RM8012 (Gold Nanoparticles, Nominal 30 nm Diameter) was used with RM8013 as representative spherical gold particles. Ammonium acetate (99.9 %, Sigma-Aldrich, St. Louis, MO, USA) was added to solutions as a volatile electrolyte for the electrospray process to generate charged aerosols from aqueous suspensions. GNR samples were first diluted in ammonium acetate to the desired concentration just prior to analysis. Electron microscopy grids (carbon and lacey carbon films) were purchased from Ted Pella (Redding, CA, USA).

Instrumentation

TEM

Transmission electron microscopy (TEM) was performed using a JEOL-2100 FEG (JEOL, Peabody, MA) with an accelerating voltage of 200 kV. To obtain the geometries of GNRs (Table 1), each aqueous GNR sample was drop-cast onto a carbon coated TEM grid. To examine the surface coating of GNRs after electrospray treatment, GNRs were selected at the peak mobility using the DMA as a bandpass filter, and directly deposited electrostatically onto a lacey carbon film for TEM imaging. Nanometer Aerosol Sampler (model 3089, TSI Inc., Shoreview, MN) was used for electrostatic deposition.

DMA-spICPMS hyphenation

GNRs were introduced to the DMA (model 3081, TSI Inc., Shoreview, MN, USA) by electrospray (ES) (model 3480, TSI Inc.) operated with a differential pressure of 2.6×10^4 Pa (3.7 psi) and using a 40 μm fused silica capillary. The DMA was operated with a sheath flow of argon at 10 L/min, and an aerosol flow of air at 1 L/min. The voltage applied to the power supply was controlled by an in-house LabVIEW software program (version 10.0.1, National Instruments, Austin, TX). The DMA step size was 2 nm with a step dwell time of 31 s. The ICP-MS (7700x, Agilent Technologies, Santa Clara, CA, USA) was operated in time resolved single particle mode with a dwell time of 10 ms. Online gas phase hyphenation of DMA to ICP-MS was achieved by a gas exchange device (GED) connected by silicone conductive tubing throughout the system. The GED was utilized to solve the incompatibility of air in the plasma. A gas exchange efficiency of about 90 % was achieved with a sweep flow of 4 L/min through the gas exchange device. For a more detailed description of the setup and operation, refer to our previous publication.[19]

Method

Basis of ES-DMA-spICP-MS in quantifying GNR dimensions

Particle mobility size is commonly expressed as an equivalent spherical diameter, (i.e., electrical mobility diameter) regardless of the actual particle shape. Electrical mobility diameter represents the diameter of a sphere that has the equivalent mobility of the analyte. For a spherical particle, the electrical mobility diameter is equivalent to its geometric diameter. However, for non-spherical particles, the measured electrical mobility diameter is a function of both particle shape and particle orientation during transit through the DMA. For simplicity, our model was built on the assumption that the GNR is a cylindrical shape with flat end-caps defined by two geometrical parameters: *viz.* diameter (d_r) and length (L_r). Although orientation of GNRs can be subject to factors such as sheath flow and aspect ratio, in addition to the applied electrical field, by operating at low voltage (i.e., < 2kV), fully random orientation is achieved. [26,27] The capacity for ES-DMA-spICP-MS hyphenation to determine d_r and L_r relies on the fact that it provides simultaneous characterization of mobility diameter, $d_{m,r}$, from DMA and mass, m_r, (or volume, v_r, if density is known) from spICP-MS ^{197}Au intensity. In this case, $d_{m,r,}$ m_r, d_r and L_r are related as follows (see also Figure S1 in the Electronic Supplementary Information, ESI):[28]

$$d_{m,r} = \left((d_r + \Delta d_{gas})(L_r + \Delta d_{gas}) + \frac{1}{2}(d_r + \Delta d_{gas})^2\right)^{\frac{1}{2}}; \quad (1)$$

$$I_r \propto m_r = \rho v_r = \rho\left(\pi\left(\frac{d_r}{2}\right)^2 L_r\right); \quad (2)$$

where I_r is the ICP-MS event intensity generated by a GNR of mass m_r. The two equations ((1) and (2)) yield two unknowns (d_r, L_r), and are therefore solvable. It is worth mentioning that the original model also added the finite diameter of the gas molecule (Δd_{gas}) to the geometry of rod. [23,29] Therefore, we added Δd_{gas} to both d_r and L_r, where inclusion of Δd_{gas} significantly improves the accuracy of the mobility model. In this case, Δd_{gas} = 2 × 0.34 nm.

The least squares method was used to search for the optimal combination of d_r and L_r, such that the calculated $d_{m,r}$ and v_r from Eq. (1)-(2) yield the best fit to the measured $d_{mr,0}$ and $v_{r,0}$. Mathematically,

$$\left(\frac{v_r - v_{r,0}}{v_{r,0}}\right)^2 + \left(\frac{d_{m,r} - d_{m,r0}}{d_{m,r0}}\right)^2 == minimum\ . \quad (3)$$

Procedure

For each GNR sample, the mass-weighted mobility size distribution was determined by DMA-ICP-MS in non-single particle mode (Figure 1(a)). The sample was then diluted to an appropriate concentration for spICP-MS measurement (i.e., from 10^5/mL to 10^8/mL). For example, the estimated concentration was 4 × 10^8/mL for CTAB-600 and 3.3 × 10^8/mL for CTAB-40-850. The limit of detection for the DMA-spICP-MS in terms of concentration and mass was described in our previous work. [19] GNRs selected at the peak mobility diameter ($d_{m,r}$) are representative of

the central tendency of the population. Experimentally, the DMA was set at a specific voltage (previously determined) corresponding to the peak mobility, for an observation time, t, during which the ICP-MS was operating in time-resolved single particle mode to detect single GNR events. Figure1 (b) shows the raw spectrum for the spICP-MS signal, each spike representing one GNR event. A standard 5σ criteria was used to distinguish particle events from the background. [30] The intensity of each spike was then converted to a frequency histogram (Figure 1(c)) to obtain the mean intensity by Gaussian fit. With appropriate calibration by reference material (NIST RM8013), the mean intensity was then converted to the mean mass (or volume, v_r) for a single GNR event. For this we calculated the mass (or volume, v_r) of RM8013 based on the reference TEM mean diameter with assumed spherical geometry. This in turn yields the volume per unit intensity and was utilized to obtain the volume of the GNR based on mean intensity from Figure 1(c). Finally, $d_{m,r}$ and v were fit using the least squares method (i.e., Eq. (3)) to obtain d_r and L_r.

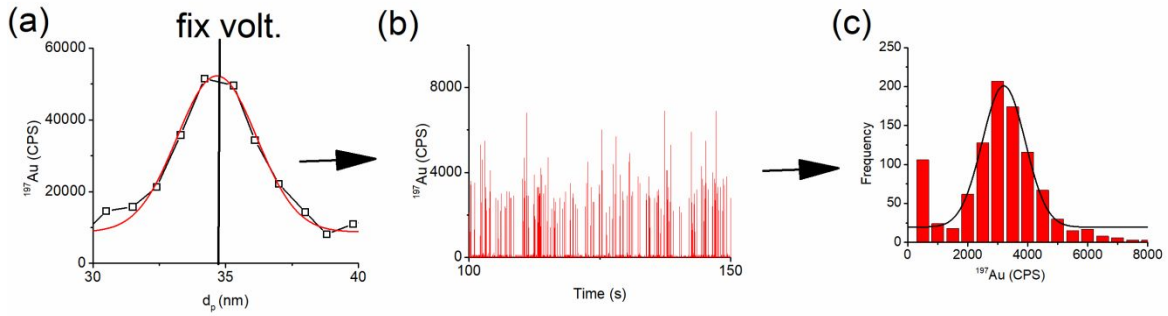

Figure 1. Procedure to determine mobility diameter ($d_{m,r}$) and volume (v_r) by DMA-spICP-MS method. (a) Intensity (volume) based mobility size distribution by DMA-ICP-MS (ICP-MS operates in non-single particle mode (t_{dwell} = 0.5 s), ^{197}Au in counts per second (CPS) was reported). Peak maximum represents the $d_{m,r}$ of the central tendency of the GNR population. For samples diluted to appropriate concentration, DMA was set at a voltage corresponding to the peak $d_{m,r}$. GNRs corresponding to this voltage were then delivered to the ICP-MS operated in single particle mode (t_{dwell} = 10 ms). (b) spICP-MS events for GNRs selected at peak $d_{m,r}$. (c) Intensity distribution for (b). Peak of the Gaussian fit to histogram in (c) was used as the mean intensity to calculate v_r.

Results and Discussion

Characterization of GNRs by TEM

A representative wide range of GNR dimensions were selected in order to validate the DMA-spICP-MS method. These dimensions include d_r (11.8 nm to 38.2 nm), L_r (47.1 nm to 151.7 nm) and AR (2 to 6.9). The surface coating and suspending medium for GNRs were reported by the vendor. The dimensions d_r and L_r were independently determined by TEM. Roughly 200 GNRs were measured for each population, with the population means and standard deviations summarized in Table 1. Representative TEM images are provided in the electronic supplementary information (ESI, Figure S2). Vendor provided d_r and L_r are also provided in the ESI (Table S1) for comparison. The relatively larger uncertainty associated with CTAB-1400 is attributed to instability / alteration in GNR size over time, since the 200 GNRs were collected and imaged at

two time points over a year apart. All other samples exhibited consistency / stable geometry within this same time frame.

Table 1. Characterization of GNRs by TEM

GNRs	Dimeter (d_r, nm)	Length (L_r,nm)	Aspect Ratio (AR)	Surface / Medium
CIT-660	17.5±1.2	47.1±6.7	2.7±0.5	Citrate / Water
CIT-800	11.9±1.3	51.4±5.3	4.3±0.6	Citrate / Water
CIT-980	11.8±1.1	70.4±9.2	6.1±1.2	Citrate /Water
CTAB-600	30.9±4.6	56.4±7.4	1.8±0.2	CTAB/3mmol/L CTAB
CTAB-20-850	20.7±1.4	89.6±12.8	4.3±0.6	CTAB/3mmol/L CTAB
CTAB-40-850	38.2±4.2	135.4±12.7	3.6±0.5	CTAB/3mmol/L CTAB
CTAB-1400	24.6±7.2	151.7±54.1	6.9±3.7	CTAB/5mmol/L CTAB

TEM evaluation of surface coating

TEM images clearly show a thin relatively low-electron-density adlayer on the GNRs (Figure 2). This coating is persistent across the majority of GNRs imaged, though occasionally it is not visible or the thickness is not uniform - it varies slightly across individual GNRs, even within the same sample. GNRs used in this study are either citrate or CTAB coated. The medium is deionized water or 3 mmol/L or 5 mmol/L aqueous CTAB. In addition to the native coating, non-volatiles (e.g., CTAB, salts) in the medium will dry onto the GNR surface during the ES process. The total dried coating thickness should be included for a complete mobility model (Eq. (1)). To sample enough GNRs for image-based analysis of the surface coating, GNRs were collected at native concentration and at the peak mobility using DMA as a band filter; however, DMA-spICP-MS measurements on these samples were, out of necessity, performed at much lower concentrations. To confirm that dilution does not significantly affect the adlayer thickness, the difference in adlayer thickness on GNRs at the native concentration and at 60× dilution was evaluated for CTAB-1400; the difference proved to be negligibly small (see Figure S3 in ESI). Based on this result, it is reasonable to assume that sampling at the native concentration is sufficiently representative of GNR coatings under conditions used for DMA-spICP-MS analysis. Mean values were obtained to estimate the thickness used in subsequent calculations (see Figure S4 (a)-(b) in ESI). Additionally, the singular contribution from non-volatiles was estimated independently based on the non-volatile peak measured by ES-DMA using a condensation particle counter (see Figure S5 in ESI).

Finally, we incorporate the thickness of the coating adlayer (Δd_{layer}) into Eq. (1) to obtain a complete mobility model:

$$d_{m,r} = \left((d_r + \Delta d_{gas} + \Delta d_{layer})(L_r + \Delta d_{gas} + \Delta d_{layer}) + \frac{1}{2}(d_r + \Delta d_{gas} + \Delta d_{layer})^2\right)^{\frac{1}{2}}$$

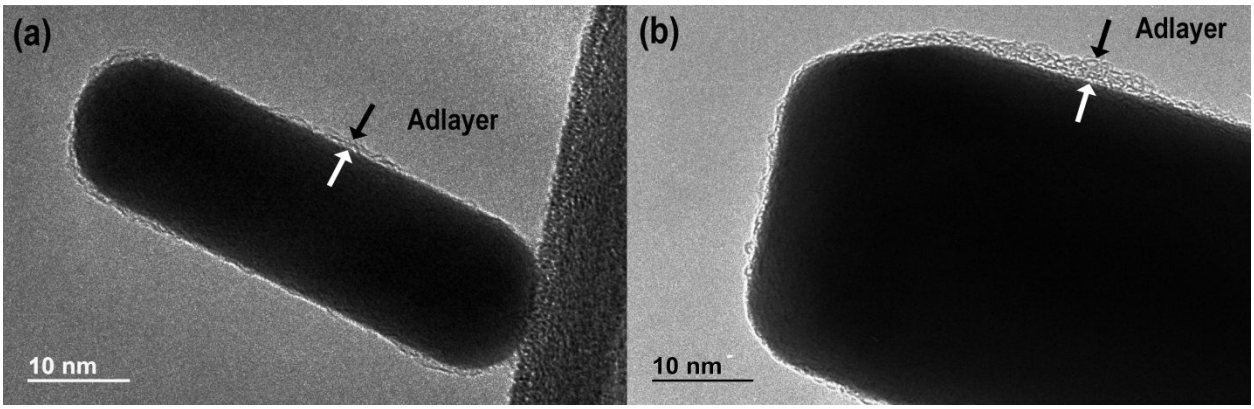

Figure 2. Two representative TEM images show evidence for a thin low density adlayer on the surface of GNRs. Both citrate and CTAB coatings were examined: (a) CIT-660 (b) CTAB-40-850

Accuracy of DMA-spICP-MS for quantitative GNR dimensions

The seven GNR samples listed in Table 1 were analyzed by DMA-spICP-MS, and the d_r and L_r were compared (see Figure 3(a)) with values directly obtained by TEM (which is used here as a benchmark). Overall, the values are consistent and comparable. Due to the nature of the method, the accuracy of measured d_r and L_r relies strongly on that of $d_{m,r}$ and v measurement. Using Eq. (1) and (2), v and $d_{m,r}$ were calculated based on d_r and L_r obtained directly from TEM (Δd_{layer} and Δd_{gas} were added to the calculation in Eq.(1)). The measured $d_{m,r}$, and v by DMA-spICP-MS was then compared with this calculated (benchmark) value and the difference reported as relative error.

$$relative\ error = \frac{(d_{m,r}\ by\ DMA-spICP-MS)\ -(d_{m,r}\ calculation\ based\ on\ TEM)}{d_{m,r}\ calculation\ based\ on\ TEM}\%.$$

The same definition was used for calculation of relative error in v. In Figure 3(b), for most of the GNRs examined, both $d_{m,r}$ and v measurements fell within a 10 % relative error range. CIT-660 and CTAB-20-850, have a relatively larger deviation in v than the other GNRs with -19 % and -14 % respectively. Another important observation is that, even though the errors in ($d_{m,r}$, v) are comparable ((7%, -1%), (3%, 9%), (-4%, -9%)) for CIT-800, CIT-980, CTAB-40-850, respectively (Figure 3(b)), the prediction of d_r and L_r based on Figure 3(a) for CIT-800 deviated from the TEM result to a larger extent (39 % in L_r and -16 % in d_r) in comparison to the other materials (e.g., CIT-980 (3 % in L_r, and 3 % in d_r), CTAB-40-850 (-10 % in L_r and 1 % in d_r)). This suggests that sensitivity of the model (robustness) to error in $d_{m,r}$ and v measurements may differ significantly based on GNR dimensions. This also suggests that the weight or importance of error in $d_{m,r}$ and v measurement might differ in their influence upon the final accuracy of the prediction of L_r and d_r. A detailed robustness analysis discussing this phenomenon is presented in the following section. It is worth noting that, despite this result, for most GNRs, d_r and L_r lie well within the one standard deviation range of TEM results (error bars represent 1σ). The relatively large error bars from TEM (average of roughly 200 GNRs) indicates the polydisperse nature of the GNR samples. It should be emphasized that the DMA-spICP-MS method described here measures the dimensions of the population central tendency and therefore has a negligible polydispersity. Finally, it is interesting to note that there is a noticeable trend for DMA-sp-ICP-MS estimates to be smaller in diameter and larger in length compare with TEM. This might

indicate a bias or systematic error of unknown origin. Though the statistical sampling is too small to support any finite conclusion here, it merits further scrutiny in future work.

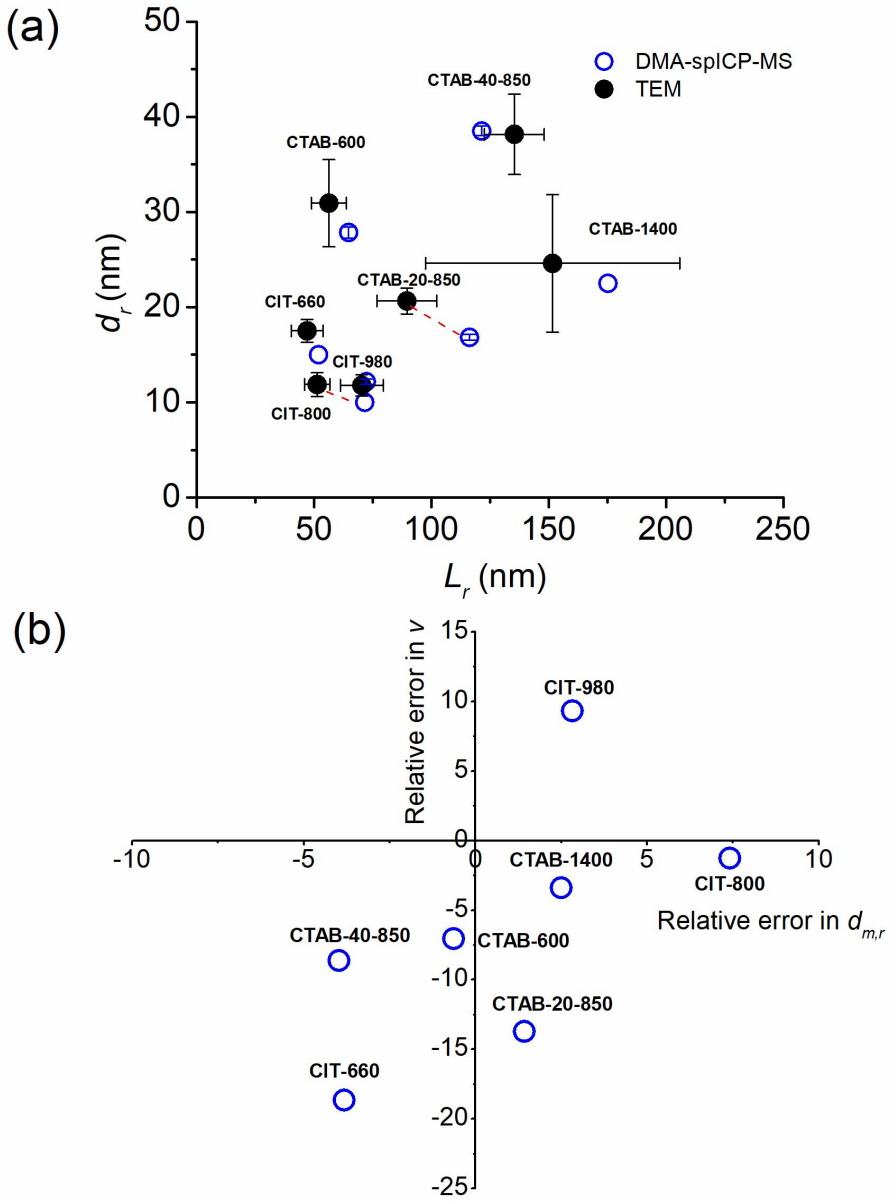

Figure 3. (a) Comparing d_r *and* L_r determined by DMA-spICP-MS (open circles) to that obtained by TEM (solid circles). Red dash lines connect data points corresponding to the same sample, in cases where the relationship may not be clear. Error bars represent one standard deviation (3 replicate measurements for DMA-spICP-MS and roughly 200 GNRs for TEM). If error bars are not visible, they are smaller than the symbol. (b) Relative error (%) in $d_{m,r}$ and v measured by DMA-spICP-MS in comparison to theoretical calculation based on TEM.

Robustness analysis

To test the method robustness, the effect of perturbation (bias or error) in each parameter (i.e., $d_{m,r}$, v and Δd_{layer}) on the final predicted d_r and L_r was evaluated. The $d_{m,r}$, v and Δd_{layer} based on TEM measurements were used as benchmarks (zero point of x-axis in Figure 4) for quantifying the extent of perturbation. When examining the perturbation of one parameter, e.g. $d_{m,r}$, the other parameters (v and Δd_{layer}) were kept at the benchmark value. A +5 % perturbation in $d_{m,r}$ is 1.05× benchmark $d_{m,r}$, while -5 % is 0.95× the benchmark value. All three parameters were then applied to our model to predict d_r and L_r. The final combined error (CE) in comparison to actual d_r and L_r in TEM was used as a quantitative metric for the method and is mathematically defined as:

$$\mathrm{CE} = \left(\left(\frac{d_r - d_{r,0}}{d_{r,0}} \right)^2 + \left(\frac{L_r - L_{r,0}}{L_{r,0}} \right)^2 \right)^{\frac{1}{2}} \quad (5)$$

Where $d_{r,0}$ and $L_{r,0}$ is the benchmark TEM diameter and length of GNRs. From the definition of CE, CE/2 represents the average error in prediction of d_r or L_r.

Figure 4(a) presents the change of predicted d_r, L_r and CE as a function of $d_{m,r}$ perturbation. Note that d_r and L_r change in the opposite direction (red and black trace) with respect to perturbation in $d_{m,r}$, while there is a minimum (valley) for CE (blue trace).

Next we evaluated the effect of perturbation in $d_{m,r}$ and v, using two GNRs with substantially different dimensions (CIT-800 with d_r of 11.9 nm and L_r of 51.4 nm, and CTAB-40-850 with d_r of 38.2 nm and L_r of 135.4 nm). In Figure 4(b), for the same percentage of perturbation in both $d_{m,r}$ and v, the latter yields a much lower final CE for the two GNRs considered. In other words, v is more resistant to perturbation in measurement compared to $d_{m,r}$, and explains why CIT-800 exhibits the largest deviation in d_r and L_r prediction, as it has the largest error in $d_{m,r}$ measurement. Meanwhile, at the same extent of perturbation in v, the larger size GNR (CTAB-40-850) exhibits a slightly higher CE. This effect is not clear for perturbation in $d_{m,r}$. Still, 0 % to 5 % perturbation in v yields a negligibly small CE (CE/2 < 6%), meaning, on average, < 6 % error in prediction of d_r and L_r. By comparison, a 0 % to 5 % perturbation in $d_{m,r}$ yields a relatively larger error in prediction (CE/2 < 23 %), meaning errors in the DMA measurement can potentially translate into significant bias relative to the true value.

Finally, the perturbation in adlayer thickness was also examined. In this case, as expected, the larger size GNR (CTAB-40-850) yields a smaller CE with respect to the same extent of perturbation (Figure 4(c)). In other words, as GNR mass/volume increases, the contribution of the relatively thin adlayer decreases.

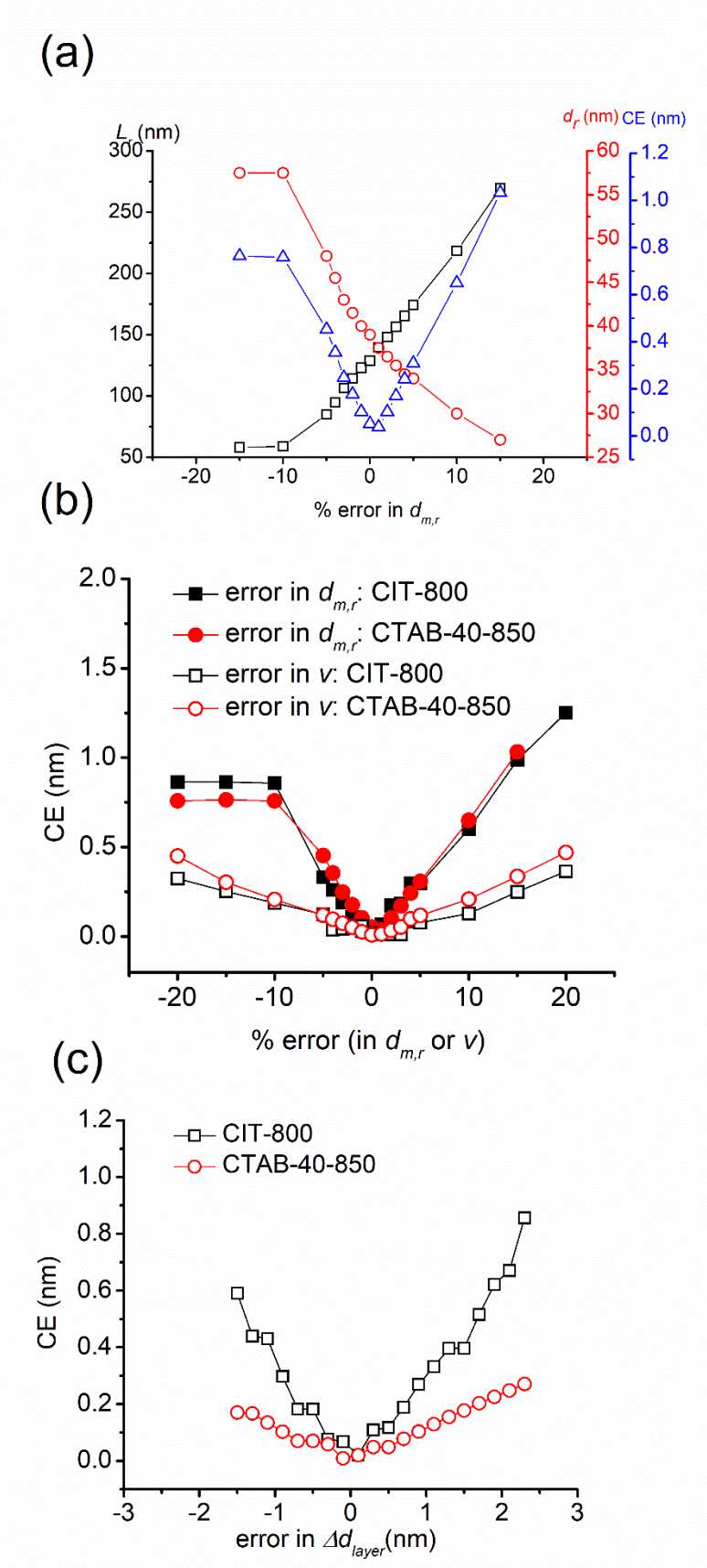
(a)
L_r (nm)
d_r (nm)
CE (nm)
% error in $d_{m,r}$
(b)
error in $d_{m,r}$: CIT-800
error in $d_{m,r}$: CTAB-40-850
error in v: CIT-800
error in v: CTAB-40-850
CE (nm)
% error (in $d_{m,r}$ or v)
(c)
CIT-800
CTAB-40-850
CE (nm)
error in Δd_{layer}(nm)

296

Figure 4. Robustness analysis of DMA-spICP-MS method. CE is defined as the combined error as defined in Eq. (5). (a) Change of L_r, d_r, and CE with respect to perturbation in $d_{m,r}$ measurement (CTAB-40-850 as an example). (b) Effect of both $d_{m,r}$ and v perturbation on CE comparing two different dimensional configurations (CIT-800 vs. CTAB-40-850). (c) Effect of adlayer Δd_{layer} on CE comparing two different geometries (CIT-800 vs CTAB-40-850).

Nanorod detection and separation based on AR

The quality and purity of synthesized GNRs is essential for critical applications, however polydisperse GNRs with undesired by-products are frequently observed in both laboratory and commercial grade materials. [24,31] From a quality control perspective, applicability of DMA-spICP-MS for such a purpose was investigated by intentionally combining GNRs having different dimensions (i.e., CTAB-20-850, CTAB-40-850 and CTAB-1400) with spheroidal gold NPs (CTAC-50). A contour plot is used to visualize and interpret the data. Prior to the construction of the contour plot, the intensity of GNRs for each spike were converted to volume (and further to diameter) using RM8013 as a calibration standard. Figure 5(a) shows that four populations can be resolved, each representing a specific geometry/size combination. The white line represents the theoretical expectation for spherical nanoparticles, where the volume based diameter d_{vol} should track linearly with the mobility diameter $d_{m,r}$. This line was constructed by linear fit to RM8012 and RM8013, the slope of which is about 0.94, meaning there is inherently a bias in mobility-based diameter versus volume-based diameter. Among the four populations, one lies very close to the white line, which corresponds to CTAC-50 spherical gold NPs. The other populations deviate from the theoretical line, a characteristic associated with non-spherical geometry. Using $d_{m,r}$ and d_{vol} from the peak of each population in our model, the d_r and L_r for each GNR are obtainable. The results for determining the GNR dimensions from the mixture are compared with that from individual measurements as well as benchmark TEM values in Figure 5(b). The adlayer thickness was considered in all cases. The d_r and L_r measured from multicomponent mixtures is in good agreement with individual measurements as well as TEM benchmark values, and therefore indicates robustness of the method. The DMA-spICP-MS method can thus distinguish spherical nanoparticles from rods, has sufficient resolution to separate GNRs with different ARs, and yields an accurate dimensional measurement for each population in a mixture.

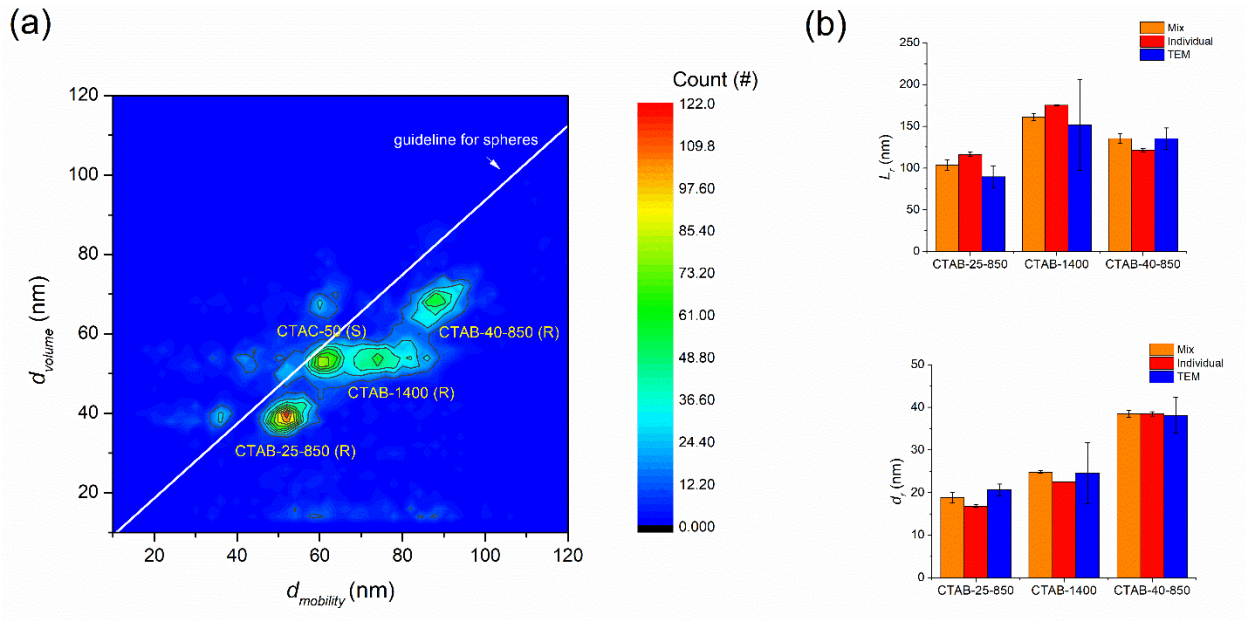

Figure 5 (a) Comparison of volume-based d_{vol} and mobility diameter $d_{mobility}$ for a mixture of GNRs and gold nano-spheres. The heat bar represents the particle counts. (b) L_r, d_r obtained from the mixture, individual GNRs and the TEM benchmark data.

In some cases, there may be no significant adlayer on the ES processed GNRs, while the gas contribution is relatively small (i.e., $\Delta d_{gas} + \Delta d_{layer} \approx 0$). For example, this may include GNRs that have no ligand functionalization, GNRs in a cleaner medium, or GNRs that can be dialyzed into a volatile buffer (such as ammonium acetate) without loss of stability. In this case, a reduced form combining equations (1)-(2) would be obtained as follows:

$$\rho = \frac{v_{mobility}}{v} = \frac{2(AR + 0.5)^{1.5}}{3AR}, \quad (6)$$

where $\frac{v_{mobility}}{v}$ is defined here as a mobility-based apparent density, ρ [19]. Theoretically, for a mixture of GNRs with different geometries or ARs, one could differentiate between the species using ρ measured by DMA-spICP-MS or alternatively use ρ to estimate the AR. The GNR samples examined in this study are not sufficiently stable after removing the solution components, and we did not have a perfect mixture of clean or non-surface functionalized GNRs available to test this relationship. Instead, for this purpose, we utilized the same rod mixture and gold nanospheres as in Figure 5(a), therefore with an expectation of measurable deviation from equation (5). The different populations have been identified as in Figure 5(a) and the peak value ($d_{mobility}$, d_{vol}) was utilized to calculate ρ (i.e., $v_{mobility} = \frac{\pi}{6} d_{mobility}{}^3, v = \frac{\pi}{6} d_{vol}{}^3$). Each population is represented by open symbols in Figure 6(a) where ρ vs. $d_{mobility}$ is presented. The blue line represents the theoretical relationship between ρ and AR based on Eq. (6). For each GNR, from the experimentally measured ρ, its corresponding AR was derived from the blue curve. Briefly, we draw a horizontal line from the center of the symbol (result) to a point where it intersects the blue line. The x value at that point is the AR (gray dotted line). The ARs obtained in this manner for the three GNR populations yielded values of about 8.1, 8.9 and 4.9 (orange bar in Figure 6 (b)).

These values correspond to CTAB-20-850, CTAB-1400 and CTAB-40-850, with TEM benchmark ARs 4.3, 6.9 and 3.6, respectively (blue bar in Figure 6 (b)). The reason for the observed deviation from the true AR is primarily due to the assumption that $\Delta d_{gas} + \Delta d_{layer} \approx 0$. If the adlayer obtained from TEM images is considered in the model, the AR obtained from Figure 5(b) using values for "mix" (orange bar), based on AR = L_r/d_r for the three GNRs, are 5.5, 6.5, and 3.5, for CTAB-20-850, CTAB-1400 and CTAB-40-850, respectively (red bar in Figure 6(b)). These values are consistent with the benchmark TEM values.

Overall, the AR differentiation within a mixture of GNRs obtained by DMA-spICP-MS measurement is deemed satisfactory, and we anticipate an improvement in agreement for samples in a cleaner medium and without the CTAB coating. Because we applied equations for a rod geometry to the spheroidal CTAC-50 gold NPs, the corresponding data point in Figure 6(a) yields a predicted AR of 2 (not 1); in this case, AR=2 is consistent with a "quasi-spherical" shape.

The slope of the blue curve represents the sensitivity of the DMA-spICP-MS method in distinguishing GNRs by their AR value. In our case, a variation of AR ranging from 1 to 10, would result in an apparent density change of roughly 1. This indicates that this method is limited in sensitivity with respect to AR determination. Regardless, the technique shows promise in its capacity for separating and distinguishing mixtures of GNRs with different dimensions and AR values, combined with a low limit of detection (≈10^5 particles/mL).[19]

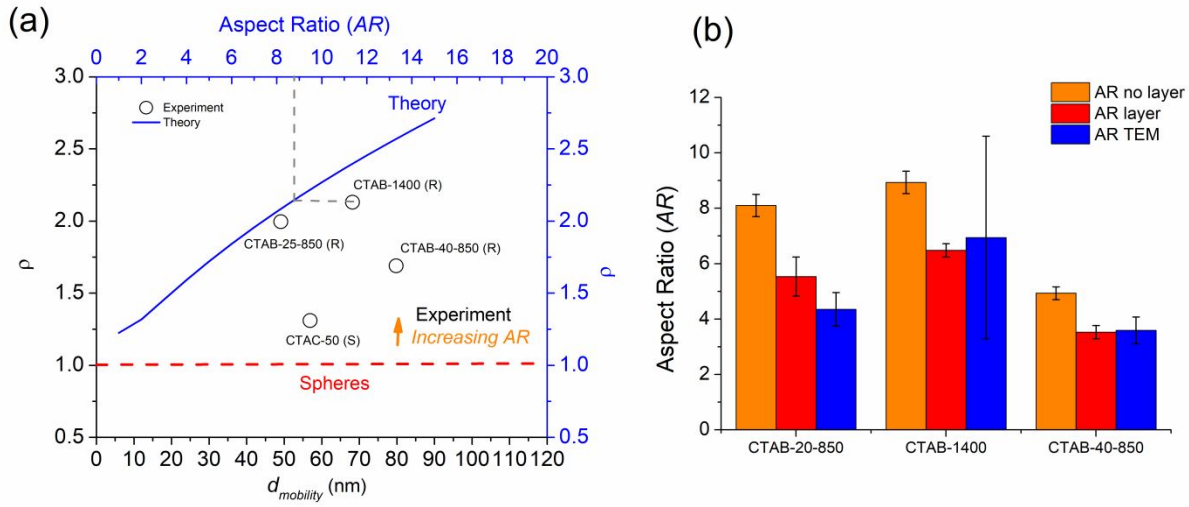

Figure 6 (a) Distinguishing mixtures of GNRs and gold spheres by AR. Hollow symbols are experimental data ($d_{mobility}$ vs. ρ). The blue line represents the theoretical relationship between AR and ρ, where ρ is unitless based on its definition (i.e. Eq. (6)). (b) Comparison of AR by three different methods: (1) AR no layer refers to AR derived from the theoretical curve as in (a), with an assumption of no adlayer. (2) AR layer refers to *AR* derived from dimensions obtained from Figure 5(b) (i.e., "mix", orange bar). (3) AR TEM is calculated from dimensions measured by TEM.

Conclusions

By combining information obtained from two orthogonal techniques operated in tandem, we have demonstrated the capacity for a novel approach, ES-DMA-spICP-MS, to simultaneously and rapidly quantify both the length and diameter of technologically important nanorods over a wide range of dimensions, and to differentiate rods from spheroidal contaminants. Commercially available gold nanorods were used to evaluate the approach. Trueness and bias were assessed by comparison with direct measurements obtained off-line using TEM imaging. Due to the nature of spICP-MS, this method has the inherent advantages of fast sampling at low particle concentrations. Because of the high resolution associated with DMA, impurities can be distinguished from rods, and rods within an extremely narrow dimensional range (i.e., single mode population) can be selected for analysis by simply varying the applied voltage. A simple rod-based mobility model was presented and assessed. The model also considers the effect of thin coatings (e.g., from surfactants or ligands). The method is limited by high levels of non-volatile solutes, which lead to thick coatings that can significantly impact the rod dimensions and shape. Additionally, the dependence on spICP-MS detection presents limitations with respect to minimum detectable mass and measurable elements (more specifically their stable isotopes); consequently, the method is applicable primarily to metals or metal containing solids. Overall, this new method should prove valuable for rapid statistically-relevant quality assessment in material development and manufacturing control of applicable asymmetric nanomaterials.

Conflicts of interest

There are no conflicts to declare.

Acknowledgements

The authors thank Prof. De-Hao Tsai (National Tsing Hua University, Department of Chemical Engineering) and Kaleb Duelge (NIST/UMD) for critical review and comments on the draft manuscript. JT was supported by a grant from NIST (award #70NANB13H021).

Notes

† The identification of any commercial product or trade name does not imply endorsement or recommendation by National Institute of Standards and Technology.

References

1. Y. Li, W. Shen, *Chem Soc Rev*, 2014**, 43**, 1543-74.
2. X. Huang, S. Neretina, M. A. El-Sayed, *Adv Mater*, 2009, **21**, 4880-910.
3. N. K. Reddy, M. Devika, C. W. Tu, *RSV Adv.*, 2014, **4**, 37563-37568.
4. A. Manekkathodi, M. Y. Lu, C. W. Wang, L. J. Chen, *Advanced Materials*, 2017, **22**, 4059-4063.
5. S. Liang, F. Teng, G. Bulgan, R. Zong, Y. Zhu, *J. Phys. Chem.*, 2008, **112**, 5307-5315.
6. D. Pissuwan, S. Valenzuela, M. B. Cortie, *Biotechnol Genet Eng Rev*, 2008, **25**, 93-112.
7. J. Cao, T. Sun, K. T. V. Grattan, *Sensors and Actuators B: Chemical*, 2014, **195**, 332-351.
8. T. B. Huff, L. Tong, Y. Zhao, M. N. Hansen, J. X. Cheng, A. Wei, *Nanomedicine (Lond)*, 2007, **2**, 125-32.
9. S. Link, M. B. Mohamed, M. A. El-Sayed*, *J. Phys. Chem. B*, 1999, **103**, 3073-3077.
10. A. Brioude, X. C. Jiang, M. P. Pileni, *J Phys Chem B*, 2005, **109,** 13138-42.

11. L. S. Slaughter, W.-S. Chang, P. Swanglap, A. Tcherniak, B. P. Khanal, E. R. Zubarev, S. Link, *J. Phys. Chem. C*, 2010, **114**, 4934-4938.
12. R. D. Near, S. C. Hayden, M. A. El-Sayed, *J. Phys. Chem. C*, 2013, **117**, 18653-18656.
13. B. N. Khlebtsov, N. G. Khlebtsov, *J. Phys. Chem.*, 2007, **111**, 11516-11527.
14. N. H. Xu, B. F. Bai, Q. F. Tan, G. F. Jin, *Optics Express*, 2013, **21**, 2987-3000.
15. B. N. Khlebtsov, V. A. Khanadeev, N. G. Khlebtsov, *J. Phys. Chem. C*, 2008, **112**, 12760-112768.
16. B. N. Khlebtsov, V. A. Khanadeev, N. G. Khlebtsov, *Phys. Chem. Chem. Phys.*, 2014, **16**, 5710-5722.
17. Z. J. Hu, S. Hou, Y. L. Ji, T. Wen, W. Q. Liu, H. Zhang, X. W. Shi, J. Yan, X. C. Wu, *AIP Advances*, 2014, **4**, 117137.
18. S. Elzey, D. H. Tsai, L. L. Yu, M. R. Winchester, M. E. Kelley, *Anal Bioanal Chem*, 2013, **405**, 2279-88.
19. J. Tan, J. Liu, M. Li, H. El Hadri, V. A. Hackley, M. R. Zachariah, *Anal Chem*, 2016, **88**, 8548-55.
20. S. Guha, M. Li, M. J. Tarlov, M. R. Zachariah, *Trends Biotechnol*, 2012, **30**, 291-300.
21. S. H. Kim, G. W. Mulholland, M. R. Zachariah, *J. Aerosol Sci.*, 2007, **38**, 823–842.
22. M. Li, R. You, G. W. Mulholland, M. R. Zachariah, *Aerosol Science and Technology*, 2014, **48**, 22-30.
23. M. Li, R. You, G. W. Mulholland, M. R. Zachariah, *Aerosol Science and Technology*, 2013, **47**, 1101-1107.
24. T. Nguyen, J. Liu, V. Hackley, *Chromatography*, 2015, **2**, 422-435.
25. Reference Material 8013, Gold Nanoparticles, Nominal 60 nm Diameter, *National Institute of Standards and Technology*, 2015.
26. A. Zelenyuk, D. Imre, *Aerosol Science and Technology*, 2007, **41**, 112-124
27 M. Li, G. W. Mulholland, M. R. Zachariah, *Aerosol Science and Technology*, 2012, **46**, 1035-1044
28 M. Li, G. W. Mulholland, M. R. Zachariah, *Physical Review E*, 2014, **89**, 022112
29 B. K. Ku, J. F. d. l. Mora, *Aerosol Science and Technology*, 2009, **43**, 241-249.
30. J. Tuoriniemi, G. Cornelis, M. Hassellov, *Analytical Chemistry*, 2012, **84**, 3965-3972.
31. T. M. Nguyen, J. M. Pettibone, J. Gigault, V. A. Hackley, *Anal Bioanal Chem*, 2016, **408**, 2195-201.

TOC

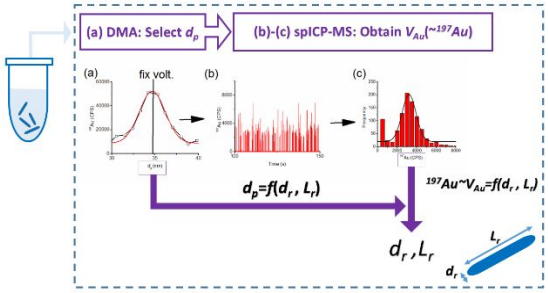

Fast, quantitative measurement of nanorod dimensions using tandem ion mobility spectrometry-single particle inductively coupled mass spectrometry.